THE JOURNAL OF PHYSICAL CHEMISTRY C

Article

pubs.acs.org/JPCC

# New Insights into the Dynamics That Control the Activity of Ceria–Zirconia Solid Solutions in Thermochemical Water Splitting Cycles

Alfonsina Pappacena,[†] Marzio Rancan,[§,‡] Lidia Armelao,[§,‡] Jordi Llorca,[∥] Wenna Ge,[⊥] Bangjiao Ye,[⊥] Andrea Lucotti,[#] Alessandro Trovarelli,[†] and Marta Boaro*[,†]

[†]Dipartimento Politecnico di Ingegneria e Architettura, Università di Udine, Via del Cotonificio 108, Udine 33100, Italy

[‡]Istituto di Chimica della Materia Condensata e di Tecnologie per l'Energia (ICMATE) − Consiglio Nazionale delle Ricerche (CNR), Corso Stati Uniti 4, Padova 35127, Italy

[§]Dipartimento di Scienze Chimiche, Università di Padova, Via Marzolo 1, Padova 35131, Italy

[∥]Institut de Tècniques Energètiques and Barcelona Research Center in Multiscale Science and Engineering, Universitat Politècnica de Catalunya, EEBE, Eduard Maristany 10-14, Barcelona 08019, Spain

[⊥]State Key Laboratory of Particle Detection and Electronics, University of Science and Technology of China, Hefei 230026, People's Republic of China

[#]Dipartimento di Chimica, Materiali ed Ingegneria Chimica "G. Natta", Politecnico di Milano, Piazza Leonardo da Vinci 32, Milano 20133, Italy

Supporting Information

**ABSTRACT:** The reactivity of a ceria-rich $Ce_{0.85}Zr_{0.15}O_2$ solid solution toward the thermochemical water splitting process (TWS) was studied over repeated $H_2/H_2O$ redox cycles. The structural and surface modifications after treatment at high temperature under air or $N_2$ atmospheres were characterized by high-resolution transmission electron microscopy (HRTEM), X-ray diffraction (XRD), Raman spectroscopy, X-ray photoelectron spectroscopy (XPS), and positron annihilation lifetime spectroscopy (PALS). Samples treated under nitrogen resulted more active due to phase segregation with formation of a zirconyl oxynitride phase in catalytic amount. Insertion of $N^{3-}$ into the structure contributes to an increase in the numbers of oxygen vacancies that preferably arrange in large clusters, and to the stabilization of $Ce^{3+}$ centers on the surface. In comparison, treatment under air resulted in a different arrangement of defects with less $Ce^{3+}$ and smaller and more numerous vacancy clusters. This affects charge transfer and H-coupling processes, which play an important role in boosting the rate of $H_2$ production. The behavior is found to be only slightly dependent on the starting ceria−zirconia composition, and it is related to the development of a similar surface heterostructure configuration, characterized by the presence of at least a ceria-rich solid solution and a (cerium-doped) zirconyl oxynitride phase, which is supposed to act as a promoter for TWS reaction. The above findings confirm the importance of a multiphase structure in the design of ceria−zirconia oxides for water splitting reaction and allow a step forward to find an optimal composition. Moreover, the results indicate that doping with nitrogen might be a novel approach for the design of robust, thermally resistant, and redox active materials.

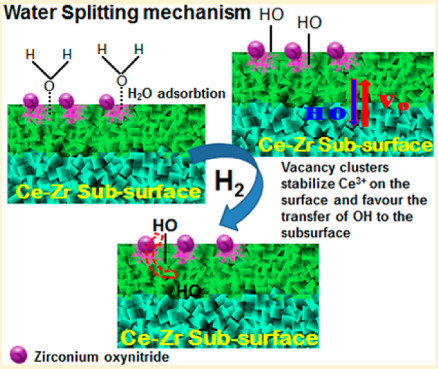


## INTRODUCTION

The necessity to increase the sustainability of modern societies requires the development of a circular economy based on an increasing use of renewable resources for the production of energy services. Solar energy and water are winning ingredients for an improvement of the energy conversion chain, which would be based on the use of hydrogen or biofuels. Among the technologies that exploit sunlight to produce fuels, solar thermochemical processes have a good potentiality in terms of efficiency, and there are excellent reviews that summarize the main outcomes in the field.[1−3] In these processes, the solar resource is used directly to drive endothermic chemical reactions such as the splitting of water (WS) and/or of $CO_2$ (CDS). Water spontaneously decomposes into elementary $O_2$ and $H_2$ only at temperature higher than 3800 °C.[3] This condition, along with the necessity of separating $O_2$ from $H_2$, makes the direct thermolysis of water impractical. However, the reaction is possible through multistep thermal cycles using specific compounds as promoters. Reducible metal oxide redox couples such as $SnO_2/SnO$, $ZnO/Zn$, $Fe_3O_4/FeO$, and $CeO_2/Ce_2O_3$ have been shown suitable to split water in two steps: an endothermic step at high temperature (∼1200−2000 °C) in which the oxide is reduced in inert atmosphere and a subsequent exothermic step at lower temperature in which

Received: June 20, 2017
Revised: July 31, 2017
Published: August 2, 2017





DOI: 10.1021/acs.jpcc.7b06043
J. Phys. Chem. C 2017, 121, 17746−17755

water oxidizes the metal oxide producing $H_2$ (~400−1300 °C).[3] The working temperature of each step, $O_2$ and $H_2$ yields, and the fuel purity strongly depend on the type of metal oxide involved. Among many metal oxides proposed in literature, ceria is one of the most promising candidates.[4] $CeO_2$ can be reduced to $Ce_2O_3$[5] or to $CeO_{2-\delta}$ (reaction 1)[4,6] with the aid of solar energy in an inert atmosphere and at high temperature (1300−1800 °C). It then can be promptly oxidized by water (reaction 2) at intermediate temperature (500−800 °C) producing pure $H_2$ on demand without purification, storage, and transport complications, as was conversely encountered in other metal oxide-based cycles.

$$CeO_2\ (s) \rightarrow CeO_{2-\delta}(s) + \delta/2O_2\ (g) \quad (1)$$

$$CeO_{2-\delta}\ (s) + \delta H_2O\ (g) \rightarrow CeO_2\ (s) + \delta H_2\ (g) \quad (2)$$

Thermodynamic studies of this cycle suggest that solar to fuels efficiency approaching 30% could be achievable, when a complete heat recovery is accomplished.[7,8] Several experimental and theoretical studies have identified in the reduction step the main limits of ceria-based cycles.[3,9] At a temperature higher than 1800 °C, which is necessary for a full reduction of $CeO_2$ to $Ce_2O_3$, $CeO_2$ starts to sublimate, and consequently the yield of cycles has been observed to decrease over time. At lower temperatures, ceria cannot be fully reduced, and $H_2$ production depends on the degree of reduction achieved. Therefore, many studies on ceria-based systems have been focused on decreasing the reduction temperature of the $Ce^{4+}/Ce^{3+}$ redox couple, while maintaining the high reactivity of reduced $Ce^{3+}$ species toward water.[3,10] The addition of $Zr^{4+}$ into the ceria lattice resulted effective in increasing the thermodynamic driving force of $CeO_2$ reduction at lower temperatures,[11,12] while aliovalent dopants have been found less effective.[13,14] New synthesis strategies to control the morphology and the sintering processes of ceria have also been adopted with success.[15] Most recently, other solutions allowed one to obtain a high and stable production of $H_2$, such as the addition of rhodium to ceria lattice as catalyst[16] or the use of a composite of $CeO_2$ and $SnO_2$ that under reducing conditions forms a stoichiometric pyrochlore phase more reactive than the nonstoichiometric $CeO_{2-\delta}$.[17]

The effect of zirconium content in the two steps water splitting reaction has been widely studied;[13,18−21] a linear increase of the reduction yields as a function of zirconium content was observed up to a content of 25 mol %, while at higher contents a stabilization of the released $O_2$ was recorded. On the other hand, ceria−zirconia-based materials showed a slow kinetics of oxidation.[3,13,21] The oxidation rate seems to be controlled by intergranular gas-phase diffusion in the material layer. In this case, improving morphological and textural properties of the mixed oxides via codoping[22] or by using different synthesis approaches[13,23] resulted beneficial due to the possibility of tuning the crystalline size, porosity structure, and composition at the nanoscale.[24] Most of the research has been focused on ceria-rich compositions, which were supposed to be structurally stable to the high temperatures adopted in the reduction step, and the attention of scientists was mainly drawn on kinetic and thermodynamic issues of the cycle. Only a few studies investigated the correlations between water splitting performance and structural/compositional modification undergone during the redox steps,[23,25] despite that it is well-known that the redox properties of the materials are markedly affected by the thermal and redox history.[26] In a recent communication, we showed that also zirconia-rich ceria−zirconia mixed oxides can be suitable for the WS process.[27] In that study, it appeared clear that phase segregation and nitridation processes, which were induced by the thermal redox cycles, might play a major role in determining the high activity. The present study investigates in more detail the WS behavior of $Ce_{0.85}Zr_{0.15}O_2$ over more cycles and compares the results with previous outcomes with the aim to find some commonalities governing the overall behavior of ceria−zirconia in thermochemical water splitting reactions. Through the use of positron annihilation lifetime spectroscopy (PALS) and other complementary techniques, we are able to describe for the first time not only the characteristics of phases but also the arrangement of defects on the surface of material when treated at high temperature under air or nitrogen-containing atmospheres. This allows us to put forward a conceivable mechanism that explains the significance of nitridation in the WS activity of ceria−zirconia oxides.

## EXPERIMENTAL SECTION

**Materials.** $Ce_{0.85}Zr_{0.15}O_2$ was prepared with a surfactant assisted precipitation method as reported elsewhere.[28] Briefly, proper amounts of $Ce(NO_3)_3{\cdot}6H_2O$ salt (Treibacher Industrie AG) and $ZrO(NO_3)_2$ liquid gel (Treibacher Industrie AG) were dissolved in demineralized water obtaining a 0.2 M solution; concentrated $H_2O_2$ (35% Sigma-Aldrich) was then added according to the molar ratio $[H_2O_2]/[\text{total metals ions}]$ equal to 3. After 45 min of continuous stirring at ambient temperature, concentrated $NH_3{\cdot}H_2O$ (28% Sigma-Aldrich) was added to obtain a pH value of 10.5. Finally, lauric acid (Sigma-Aldrich), using a molar ratio ([total metal ions]/[lauric acid]) equal to 0.25, was directly added and maintained under continuous stirring for 4 h. The precipitate was then filtered and washed three times with 0.5 L of demineralized water, and the resulting cake was dried at 100 °C overnight. The dry precipitate was calcined in air at 500 °C for 4 h. This method allows one to obtain highly homogeneous starting materials, which ensures a reproducible phase segregation. To simulate the aging effect undergone during the strongly endothermic step of TWS cycle, the oxide was treated at 1300 °C in nitrogen or air for 4 h. Other thermal treatments in air were made at 800 °C/4 h and at 1100 °C. All of the samples were cooled in the atmosphere of treatment and exposed to air at room temperature before the reactivity tests.

**Reactivity Tests.** The experimental conditions have been chosen on the basis of previous studies.[20,23] The activity of $Ce_{0.85}Zr_{0.15}O_2$, calcined at 1300 °C/4 h either in $N_2$ (CZ85_$N_2$) or in air (CZ85_air), was evaluated toward a two-step water splitting thermal cycle using two different setups. Reduction degree of the material in $N_2$/air atmosphere was measured in a thermogravimetric analyzer (Q600-TA Instruments). The thermally aged samples (25 mg) were heated at 10 °C/min in $N_2$ flow (100 mL/min) up to 1300 °C. The oxygen released from the oxide was evaluated from the weight loss observed during 80 min of isotherm at 1300 °C. The water splitting (WS) activity was evaluated in a Micromeritics apparatus using the same method as described by Pappacena et al.[27] Each sample (50 mg) was previously reduced to obtain the same reduction degree achieved in the first endothermic step by using a 5% $H_2$/Ar flow and a heating ramp of 10 °C/min up to 700 °C. These conditions have been established through a thermogravimetry analysis (TGA, Q500-TA Instruments) in 5% $H_2$/Ar flow by reducing the sample up


DOI: 10.1021/acs.jpcc.7b06043
J. Phys. Chem. C 2017, 121, 17746−17755

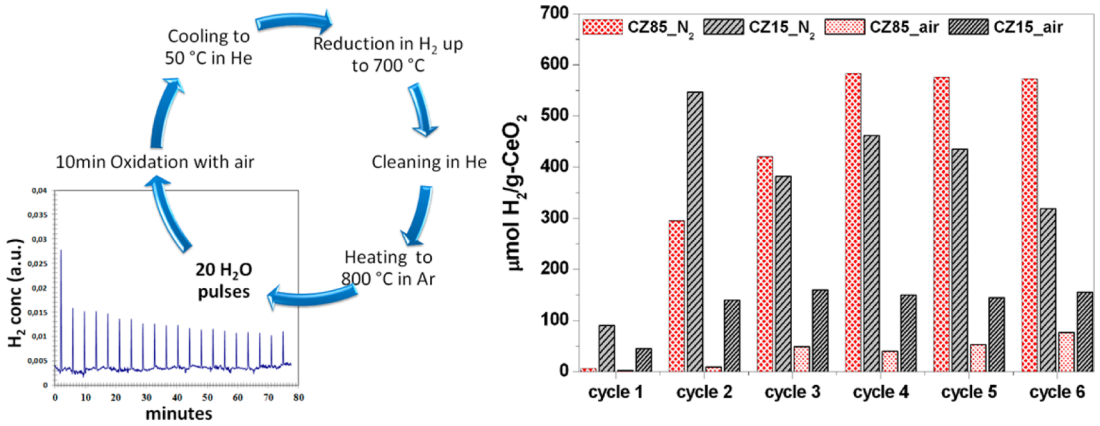


**Figure 1.** Comparison between water splitting reactivity of CZ85 and CZ15[27] pretreated in $N_2$ or air at 1300 °C/4 h. On the right is shown a schematic of one typical cycle.

to 900 °C. The reduced sample was evacuated in He and oxidized by 20 pulses of water vapor (30% in Ar flow) at 800 °C. $H_2$ consumption and production were monitored with a thermal conductivity detector; the total $H_2$ production was measured by calculating the $H_2$ outcome from the first 20 water vapor pulses. At the end of the WS reaction, the sample was oxidized with air for 10 min to complete the oxidation and cooled to ambient temperature in He atmosphere. The cycle was repeated six times. The same experiment was carried out also without completing the oxidation with air to verify whether the oxidation conditions may affect the reaction of water splitting.

**Characterization.** Structural and surface properties of all materials were investigated through the use of several techniques. X-ray diffraction analysis (XRD) was performed using a Philips X'Pert diffractometer operated at 40 kV and 40 mA equipped with a nickel-filtered Cu $K_\alpha$ radiation. All spectra were collected using a step size of 0.02° 2$\theta$ and a counting time of 40 s per angular abscissa in the range of 20−145° 2$\theta$. The Philips X'Pert HighScore software was used for phase identification. The mean crystalline size was estimated from the full width at the half-maximum of the X-ray diffraction peaks using Scherrer's equation[29] corrected for the instrument line broadening. Rietveld refinement of XRD spectra was performed by means of the GSASEXPGUI program.[30,31]

Raman spectra have been recorded with a LABRAM HR800 equipped with a solid-state laser (Laser XTRA, Toptica Photonics) operating at 785 nm and a Peltier cooled CCD detector. The laser radiation was filtered by an interference filter and was focused on the sample through an Olympus BX41 microscope. A 50× Olympus objective (NA = 0.75) has been used. The Rayleigh radiation was rejected using notch filters. To ascertain the absence of artifacts, the spectra have been obtained also using excitation radiations at 512 and 633 nm and two different grids (600 lines/mm; 1800 lines/mm).

High-resolution transmission electron microscopy (HRTEM) was accomplished with a JEOL J2010F instrument equipped with a field emission electron source and operated at 200 kV. Samples were dispersed in alcohol, and a drop of the suspension was placed over a grid with holey-carbon film.

Specific surface area (SA) and porosity of oxides were measured by nitrogen adsorption/desorption isotherms at 77 K, following the BET and BJH methods, respectively,[32] using a Tristar 3000 gas adsorption analyzer (Micromeritics). The pore size distribution was calculated from the desorption branch of the isotherm.

XPS was used as the main tool to assess the surface chemical composition of the samples before and after the catalytic process. Analyses were performed on a PerkinElmer Φ 5600-ci spectrometer using nonmonochromatized Al K$\alpha$ radiation (1486.6 eV). The spectrometer was calibrated by assuming the binding energy (BE) of the Au 4f7/2 line at 83.9 eV with respect to the Fermi level. The standard deviation for the BE values was ±0.2 eV. Survey scans were obtained in the 0−1300 eV range (187.8 eV pass energy, 0.4 eV step$^{-1}$, 0.05 s step$^{-1}$). Detailed scans were recorded for the C 1s, O 1s, Zr 3d, Ce 3d and N 1s regions (23.5 eV pass energy, 0.1 eV step$^{-1}$, 0.1 s step$^{-1}$). The BE shifts were corrected by assigning to the C 1s peak associated with adventitious hydrocarbons a value of 284.8 eV.[33] The analysis involved Shirley-type background subtraction, nonlinear least-squares curve fitting adopting Gaussian−Lorentzian peak shapes, and peak area determination by integration.[34] The atomic compositions were evaluated from peak areas using sensitivity factors supplied by PerkinElmer, taking into account the geometric configuration of the apparatus.[35] The experimental uncertainty on the reported atomic composition values does not exceed ±5%.

Positron annihilation lifetime spectroscopy experiments (PALS) were carried out with a fast-slow coincidence system, which has a resolution of 230 ps. The scintillation detectors are plastic scintillator coupled with photomultipler tubes. A 40 $\mu$Ci $^{22}$Na source of positron was sandwiched between two pieces of identical samples. For each spectrum, about 2 × $10^6$ coincidence counts have been recorded to ensure the repeatability of the measurements. The positron lifetime data were analyzed by the Lifetime9 program with the necessary source corrections.

## RESULTS

**Reactivity Results.** The endothermic step corresponding to the thermal reduction was evaluated via thermogravimetry by measuring the weight loss of the sample treated at 1300 °C in $N_2$ or air. $O_2$ released during the thermal treatment was 276 $\mu$mol/g and 169 $\mu$mol/g, respectively, for the sample aged in $N_2$ and air, which corresponds to a degree of $Ce^{4+}$ reduction of 21 and 13 mol %. Similar results were reported in the literature, but generally using higher temperature.[19,20]

Figure 1 shows the results obtained in the exothermic water splitting experiment for both the $N_2$-treated oxide and the


DOI: 10.1021/acs.jpcc.7b06043
J. Phys. Chem. C 2017, 121, 17746−17755

sample aged in air. A total of 6 cycles are reported, and the detail for one cycle is shown to the right of the image. The $N_2$-treated sample is more active, and the $H_2$ production increases significantly up to a stable value obtained with the fourth cycle. A comparison with results obtained on $Ce_{0.15}Zr_{0.85}O_2$ indicates that, regardless of initial composition, $H_2$ yields reach close values for the two nitrogen-pretreated compositions after a few cycles.[27] To exclude the role of oxygen in the promotion of $H_2$ production observed from the second cycle, the same experiment was repeated without oxidizing the samples with air at the end of each cycle, and the results are compared in Figure S1.

**Characterization Results.** Table 1 summarizes the textural and morphological properties of $Ce_{0.85}Zr_{0.15}O_2$ after thermal treatment in the range of temperatures 500−1300 °C. The material shows a good thermal stability up to 800 °C; higher temperatures cause a large drop in surface area with values close to 1 $m^2/g$ after calcination at 1300 °C, regardless of the gas type used in the treatment. Correspondingly, an increase of average crystallite size up to 40 nm with loss of porosity is found.

**Table 1. Characteristics of $Ce_{0.85}Zr_{0.15}O_2$ after the Thermal Treatments**

| calcination temperature (°C) | treatment atmosphere | specific surface area ($m^2/g$)[a] | pore size (Å) | crystallite size (Å)[b] |
|---|---|---|---|---|
| 500 | air | 94 | 238 | 54 |
| 800 | air | 45 | 345 | 99 |
| 1100 | air | 9 | ND | 275 |
| 1300 | air | 1 | ND | 425 |
| 1300 | nitrogen | 1 | ND | 403 |

[a]According to BET method. [b]Determined by the Sherrer equation from XRD analysis. ND: not determined.

The structure of the samples was investigated at the nanoscale through XRD, Raman spectroscopy, and HRTEM.

Figure 2 shows the corresponding X-ray diffraction profiles of the samples. After calcination at 500 °C, the sample crystallizes in a cubic fluorite structure with a unit cell value of 5.3652(5) Å. This value is lower than that measured for a pure ceria sample, 5.4118(1) Å, and indicative of the insertion of $Zr^{4+}$ into the ceria lattice. The application of the Vegard law[36] allows us to calculate a molar doping of zirconium equal to 0.167, which is very close to the nominal composition of the starting material. No large differences exist among the XRD profiles except for the narrowing of the peaks with the increase of the calcination temperature, indicating sintering of crystallites as a consequence of the thermal treatments.[37] However, a careful evaluation of the profiles of samples treated at 1300 °C in both air and nitrogen evidences a tiny shift ($2\theta = 0.12 \pm 0.4°$) of the most intense peak (111) of CZ85 to higher angles and a small shoulder at $2\theta = 28.10°$, thus indicating the occurrence of phase segregation accompanied by small changes in the composition of the cubic CZ85 phase. The small peak at $2\theta = 28.10°$ is attributable to the presence of a monoclinic zirconia-rich phase ($Ce_{0.05}Zr_{0.95}O_2$, PDF 88-2392). The XRD profile of the samples sintered in air shows also a small peak at $2\theta = 29.83°$, which is probably related to a tetragonal zirconia-rich phase ($Ce_{0.18}Zr_{0.82}O_2$, PDF 80-0785) or to tetragonal $ZrO_2$ (JCPDS 01-080-0785). Such type of segregation is consistent with what is reported in the literature for similar compositions.[38]

Figure 3 shows the Raman spectra of samples treated at 1300 °C before and after WS cycles. Figure S2 shows also the spectra collected using excitation lines at 512 and 633 nm. Spectra in the region 180−800 $cm^{-1}$ are characterized by an intense signal at ca. 476 $cm^{-1}$ corresponding to the fundamental vibration mode $F_{2g}$ of the fluorite structure and satellite bands at 300 and 602 $cm^{-1}$, consistent with a distortion of the cubic structure and the presence of a tetragonal t″ phase.[39] The minority phases are not detectable, and the spectra of the samples before and after WS cycles are almost identical. Above 1000 $cm^{-1}$, all

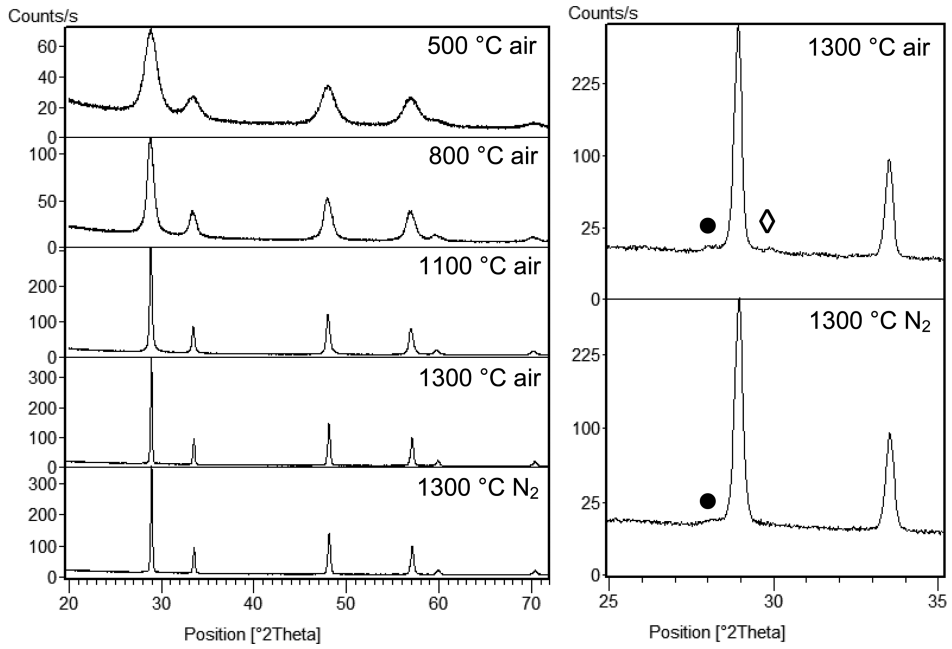


**Figure 2.** X-ray profiles of $Ce_{0.85}Zr_{0.15}O_2$ calcined at different temperatures in air and at 1300 °C in $N_2$ flow. To the right are shown details of samples treated at 1300 °C/4 h. Symbols indicate the segregated crystal phases: ●, $Ce_{0.05}Zr_{0.95}O_2$ (PDF 88-2392); ◊, $Ce_{0.18}Zr_{0.82}O_2$ (PDF 80-0785).



DOI: 10.1021/acs.jpcc.7b06043
J. Phys. Chem. C 2017, 121, 17746−17755

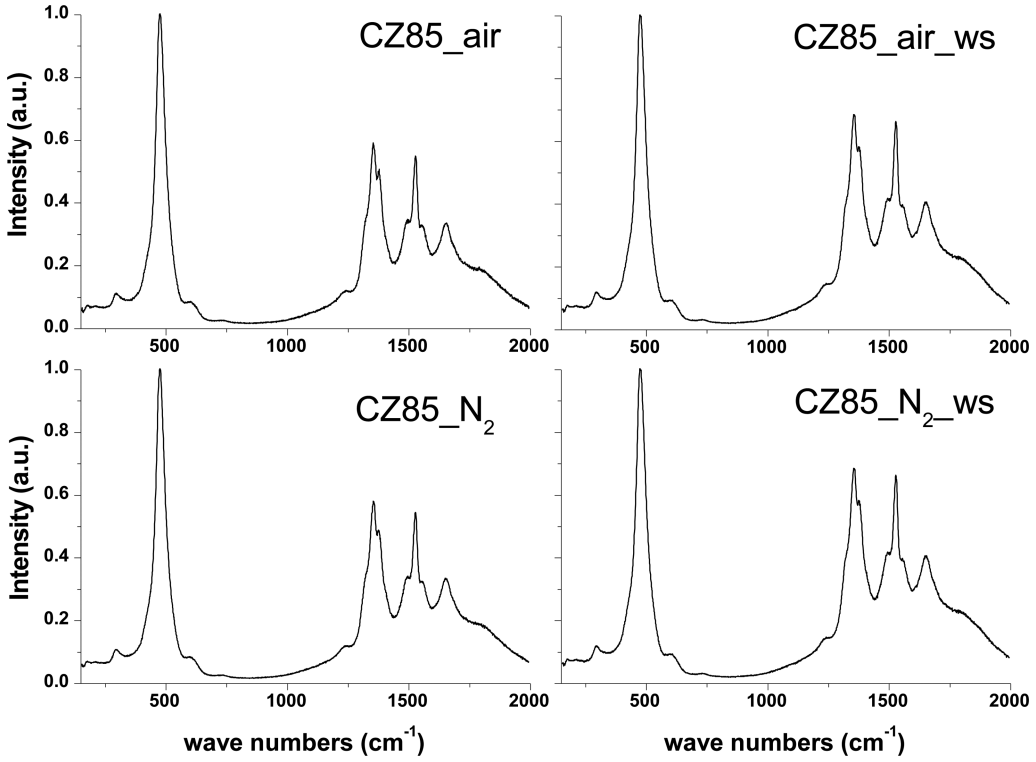


**Figure 3.** Raman spectra of CZ85 treated in air before (CZ85_air) and after six water splitting cycles (CZ85_air_ws) or in $N_2$ before (CZ85_$N_2$) and after six water splitting cycles (CZ85_$N_2$_ws). Spectra were collected using an excitation radiation at 785 nm.

of the spectra show complex bands, which are generally attributable to electronic f−f transitions of $Ln^{3+}$ ions present as impurities in the materials.[38] Alternatively, these bands have been also associated with the presence of $Ce^{3+}$ ions.[39−42] It is interesting to note that the intensity of these bands, which is generally related to the asymmetry of the sites, increases after the cycles.

Figure 4A shows an HRTEM image of the sample treated in nitrogen at high temperature. The crystallite labeled "a" corresponds to a single cubic CZ particle oriented along the [110] crystallographic direction. Spots at 3.0 Å correspond to the cubic (111) planes. In contrast, the crystallite labeled "b" shows a FT pattern exhibiting spots aligned at 2.5 and 5.1 Å as well as spots at 2.9 Å. The spots aligned at 2.5 and 5.1 Å are ascribed to the (400) and (200) crystallographic planes of $Zr_2ON_2$, respectively, whereas those at 2.9 Å correspond to the (222) planes of $Zr_2ON_2$.

These results are in good agreement with those reported in the literature,[43] except for tiny differences that could be explained with the insertion of cerium in the structure. This hypothesis is reasonable considering that $Ce^{3+}$ (103 pm) has an effective ionic radius similar to that of $La^{3+}$, and that the formation of $LaZrO_2N$ has been demonstrated.[44] The HRTEM analysis of sample treated in air (Figure 4B) does not evidence the presence of the oxynitride phase. The FT image with spots at 3.0 Å corresponds to the (111) planes of cubic CZ, which is the dominant phase. The effects of WS cycles at the nanoscale are shown in Figure 4C. The TEM image (left) evidences a sample constituted by crystallites measuring more than 100 nm in a compact arrangement, suggesting that the sample sintered during the cycles. Triple junctions are easily recognized, which usually appear upon high temperature calcination treatments. The figure at the right corresponds to a representative HRTEM

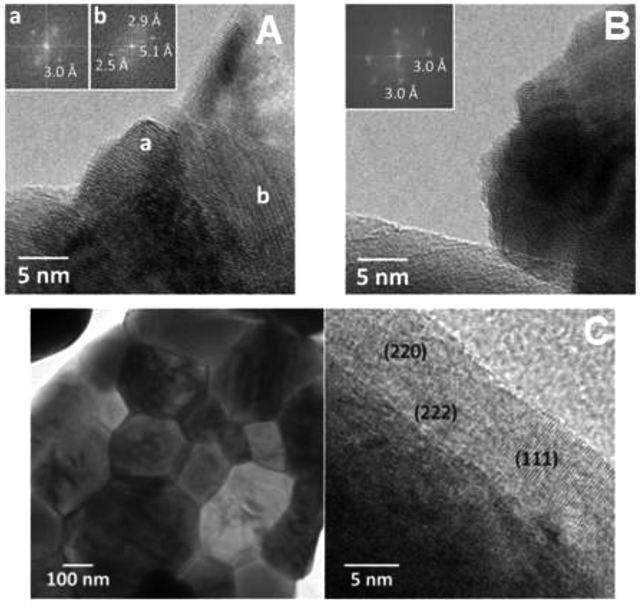


**Figure 4.** HRTEM of $Ce_{0.85}Zr_{0.15}O_2$ (CZ85) treated at 1300 °C/4 h: (A) in $N_2$, (B) in air, and (C) images of the sample treated in $N_2$ after the water splitting test.

image of the sample. In this case, only lattice fringes corresponding to the CZ oxide are recognized. In the figure, several lattice fringes are indicated and correspond to the (111), (220), and (222) crystallographic planes of cubic CZ at 3.0, 1.8, and 1.5 Å, respectively.

The composition and defects structure of samples before and after WS cycles are investigated through XPS and PALS techniques. Figure 5A and B shows the XPS spectra and the


DOI: 10.1021/acs.jpcc.7b06043
J. Phys. Chem. C 2017, 121, 17746−17755

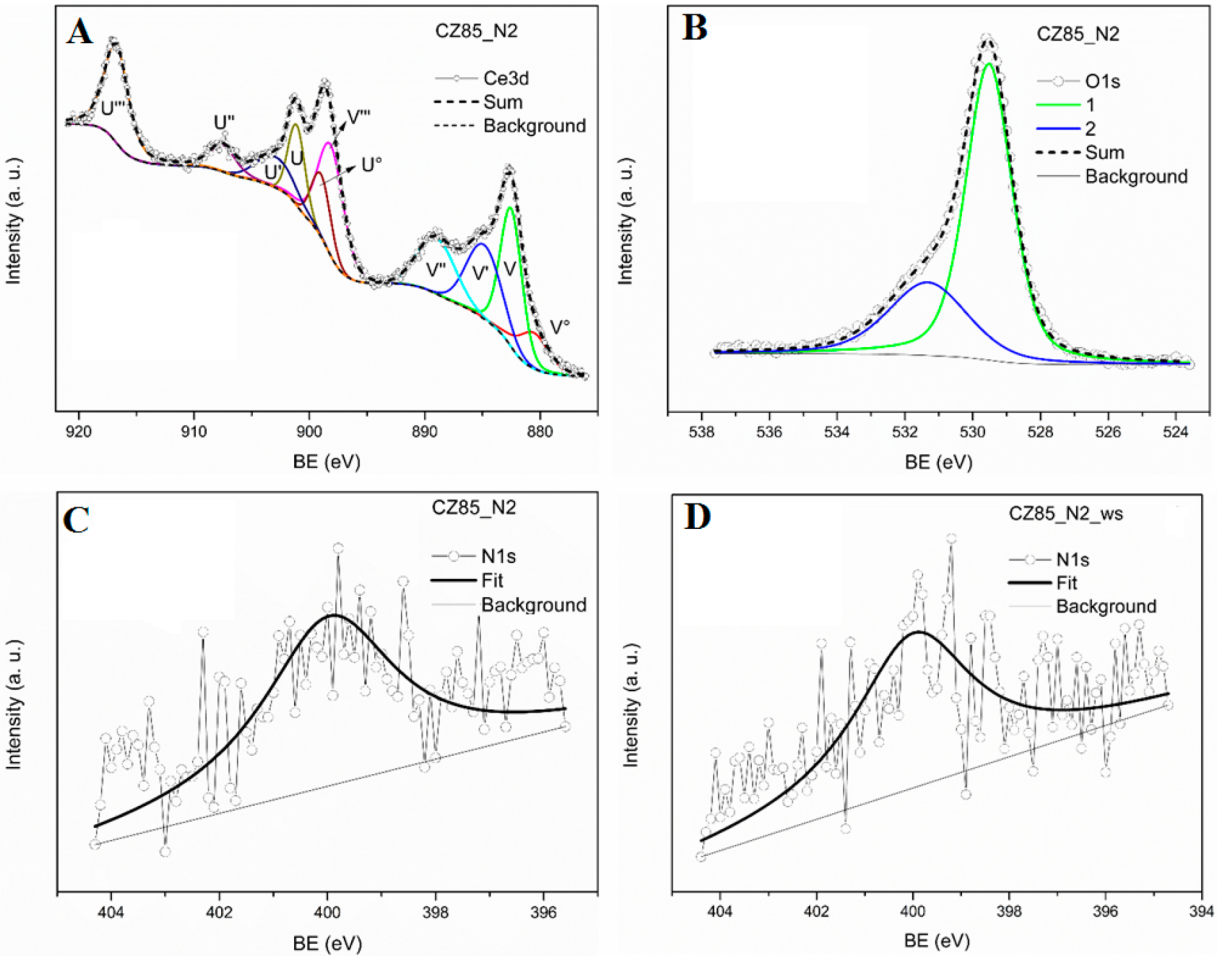


**Figure 5.** XPS spectra of CZ85 treated in $N_2$ 1300 °C/4 h. Shown are the Ce 3d, O1, and N 1s regions and related fitting components.

corresponding fitting components of Ce 3d and O 1s regions for the samples treated at 1300 °C in nitrogen. Similar features were observed for the air-treated sample and for the samples after six WS cycles (see Figures S3 and S4). Figure 5C and D shows the N 1s region of the sample treated in nitrogen before and after WS cycles.

In Figure 5A, U and V refer to cerium $3d_{3/2}$ and $3d_{5/2}$ spin−orbit components, respectively. U, U″, U‴, V, V″, and V‴ refer to the final states of $Ce^{4+}$, while U°, U′ and V°, V′ refer to those of $Ce^{3+}$.[25] The fitted peak areas were used to estimate the relative amount of $Ce^{3+}$ and $Ce^{4+}$ (see Table 2). The O 1s region is suitably fitted with two components (Figure 5B). The main component (peak 1) at about 529.5 eV is associated with the cerium−zirconium oxide matrix, while the component centered at 531.5 eV (peak 2) can be ascribable mainly to surface hydroxyl groups.[44,45] The signal N 1s at 399.9 eV (Figure 5C) confirmed the insertion of nitrogen into the surface of the CZ85_$N_2$ sample and the formation of a zirconyl oxynitride phase.[27,46,47] In addition, the evidence of the same nitrogen peak on the CZ85_$N_2$ surface after WS cycles (CZ85_$N_2$_ws, Figure 5D) indicates that the oxynitride phase is stable under WS conditions. No signal corresponding to insertion of nitrogen is observed for samples treated under air.

Table 2 summarizes the surface chemical composition (atomic %) of the samples, determined from the analysis of Ce 3d and Zr 3d XPS peaks.

Samples calcined at 500 and 1100 °C show a surface composition consistent with the nominal stoichiometry of the $Ce_{0.85}Zr_{0.15}O_2$ solid solution revealing that the starting material was homogeneous and thermally stable up to 1100 °C. After treatment at 1300 °C, the value of the Zr/Ce ratio increased to 0.26 in agreement with the phase segregation observed by XRD and indicating that zirconia-rich compositions are mainly located on the outer part of the crystallite. The presence of $Ce^{3+}$ in the starting material (500 °C) is due to the nanometric nature of the powder and to the presence of extrinsic defects induced by the zirconium doping.[38] Besides, a small quantity of $Ce^{3+}$ could be generated by the reduction of $Ce^{4+}$ under the X-ray irradiation during XPS analysis.[48] The amount of $Ce^{3+}$ increased after calcination at 1100 and 1300 °C as expected from the state diagrams of $CeO_2$ in air and $N_2$ conditions, for which $CeO_2$ starts reducing above 1000 °C.[4,6] After water

**Table 2. Results of XPS Analysis**

| sample | Ce[b] [$Ce^{3+}$, $Ce^{4+}$][c] | Zr[b] | Zr/Ce | $Ce^{3+}/Ce^{4+}$ |
|---|---|---|---|---|
| CZ85-500[a] | 84.2 [14.3, 69.9] | 15.8 | 0.19 | 0.20 |
| CZ85-1100[a] | 85.4 [22.2, 63.2] | 14.6 | 0.17 | 0.35 |
| CZ85_air | 79.0 [22.1, 56.9] | 21.0 | 0.26 | 0.39 |
| CZ85_$N_2$ | 79.1 [24.5, 54.6] | 20.9 | 0.26 | 0.45 |
| CZ85_air_WS | 79.8 [18.4, 61.4] | 20.2 | 0.26 | 0.30 |
| CZ85_$N_2$_WS | 79.1 [24.5, 54.6] | 20.9 | 0.26 | 0.45 |

[a]The number indicates the temperature of calcination in air. [b]The uncertainty on the quantitative values does not exceed ±5%. [c]Values obtained from fitting of the Ce 3d region.



DOI: 10.1021/acs.jpcc.7b06043
J. Phys. Chem. C 2017, 121, 17746−17755

splitting cycles, the concentration of $Ce^{3+}$ remained the same for the sample treated in nitrogen, while it slightly decreased in the case of the sample pretreated in air. For the $N_2$ treated sample, the extent of surface nitridation was determined from the N/Ce atomic ratio, which resulted similar before and after the WS reaction, with a value of ca. 0.03. However, due to the very low intensity of the N 1s peak, this is only a rough estimate.

Details into the organization of surface defects were obtained via positron annihilation lifetime spectroscopy (PALS). Figure S5 shows the PALS spectra for some representative sample. All spectra were fitting to three lifetime components ($\tau_1$, $\tau_2$, $\tau_3$), and the corresponding values along with their relative intensity ($I_1$, $I_2$, $I_3$) are summarized in Table 3. As far as we know, this is the first time that the PALS technique is applied to the characterization of CZ85 mixed oxides; therefore, we used a CZ85 sample calcined at 1100 °C as a reference material for an interpretation of the data. Because the temperature used for treatment is not enough high to cause phase segregation and thermal reduction, such a sample is representative of a homogeneous highly sintered composition.

**Table 3. Peak-Fitting Results of PALS Spectra**[a]

| sample | $\tau_1$ (ps) | $\tau_2$ (ps) | $\tau_3$ (ns) | $I_1$ (%) | $I_2$ (%) | $I_3$ (%) |
|---|---|---|---|---|---|---|
| CZ85_air | 170.8 | 310.0 | 1.09 | 78.9 | 20.8 | 0.35 |
| CZ85_$N_2$ | 175.2 | 358.0 | 1.02 | 72.2 | 26.6 | 1.20 |
| CZ85_$N_2$_ws | 173.7 | 351.0 | 1.83 | 83.9 | 15.5 | 0.53 |
| CZ85_air_ws | 164.4 | 291.0 | 1.40 | 74.6 | 25.0 | 0.44 |
| CZ85-1100 | 179.1 | 359.0 | 0.95 | 47.2 | 51.9 | 0.88 |

[a]Spectra fitted with the Lifetime9 software.

The longest component $\tau_3$ is attributed to the annihilation of orthopositronium atoms formed in the large voids present in the material.[49] It hardly helps in giving some useful information on defects in the samples because the formation of the orthopositronium atoms is not related to the positron trapping at defects, so it will be neglected in the following discussion. The component $\tau_1$ is generally attributed to the free annihilation of positrons in defect-free crystal. However, for disordered systems, it may also be associated with small defects (like mono vacancies) and shallow positrons traps (like oxygen vacancies), which can decrease the average electron density and elongation of $\tau_1$.[50,51]

In many studies on ceria-based oxides in the form of nanopowders, this first component $\tau_1$ has been related to neutral oxygen monovacancies associated with $Ce^{3+}$ ($Ce'_{Ce}V^{\cdot\cdot}_{O}Ce'_{Ce}$) according to Krögel−Vink notation.[52] From Table 3, we can see the $\tau_1$ values are about ∼175 ps, which are far lower than that reported in the literature, indicating that the small vacancies have higher electron density in our samples. Such a difference might be due to the fact that, in our case, the material has a larger crystal size due to its sintering at high temperature.[51] The component $\tau_2$ is much larger than the component $\tau_1$, and it arises from positrons trapped by larger size defects. These types of defects mainly locate on the surface or subsurface, and thus $\tau_2$ should give useful information on the surface defects of samples.[52−54]

It is worth noting that the values of $\tau_1$ and $\tau_2$ for the reference sample CZ85-1100 are very similar to the respective life times for the sample treated in nitrogen before the test (CZ85_$N_2$). Conversely, the related intensities $I_1$ and $I_2$ are different, and the thermal treatment in nitrogen leads to a decrease of the number of large size clusters on the surface with respect to the reference. The sample treated in air (CZ85_air) shows a lower value of $\tau_2$. Taking into account that the electron density is lower in the large size clusters rather than in the small defects, and consequently the positron lifetime increases in the larger size defects, it is inferred that in the air-treated sample the clusters of defects are smaller than those in the $N_2$-treated sample or in the reference. Moreover, by comparing the ratio $I_1/I_2$ of the two samples heated at 1300 °C, it is clear that the material treated in nitrogen has a higher cluster density than that treated in air.

After WS cycles, both of the samples treated in nitrogen and in air showed lower values of $\tau_1$ and $\tau_2$. The entity of the decrease is more significant for the sample treated in air (CZ85_air_ws) rather than for the sample treated in nitrogen (CZ85_$N_2$_ws). Opposite trends have been observed for the value of $I_2$ in the two samples. After cycles, the value of $I_2$ diminished 37% for the CZ85_$N_2$_ws, while it increased 20% for the CZ85_air_ws. That implies respectively a lower or higher number of defect clusters in the two samples after reaction.

## DISCUSSION

The results indicate that thermal treatment either in $N_2$ or in air at high temperature of $Ce_{0.85}Zr_{0.15}O_2$ induces subtle structural changes promoting phase segregation. The material treated under nitrogen shows the formation of a zirconia-based oxynitride phase located at the outer part of the grains that is beneficial for the water splitting reaction. The active phase is composed of this oxynitride phase, which is present in catalytic amount and by a pseudocubic oxide rich in ceria ($Ce_xZr_{1-x}O_{2-\delta}$, $0.7 \leq x \leq 0.9$) as a major phase. This study uses XPS and PALS to obtain more details into the defect organization of these heterogeneous structures to see how the structure and quantity of oxygen vacancies can help in developing more stable and robust WS catalysts.

In agreement with previous observations, our findings confirmed that the main surface defects in ceria−zirconia oxide are polarons, which are related to $Ce^{3+}$ centers and oxygen vacancies.[55] XPS analysis accounts for the number of $Ce^{3+}$ (Table 2), while the PALS technique gives information on the organization of oxygen vacancies (Table 3). The material treated in nitrogen shows a higher concentration of $Ce^{3+}$ and larger oxygen vacancy clusters at its surface in comparison to the sample treated in air. Moreover, the configuration of these defects remains almost the same after redox cycles (the same amount of $Ce^{3+}$ and the same cluster dimensions, even if the cluster number decreased). Conversely, the sample treated under air shows a new arrangement of defects with the presence of smaller and more numerous vacancy clusters and a decreased amount of $Ce^{3+}$ at the surface. Because the thermal treatments in nitrogen or air caused similar structural and compositional changes in the material, the different configuration of vacancies in air and $N_2$ treated materials has to be related to the nitridation process and the initial reduction degree of the two materials. Assuming that charge neutrality has to be preserved, the substitution of $O^{2-}$ anions with $N^{3-}$ must be balanced by the introduction of oxygen vacancies.[56] The addition of these extra vacancies along with the necessary vacancies to balance $Ce^{3+}$ charges (more numerous in the sample treated in nitrogen because more reduced) may justify the formation of larger vacancy clusters in the sample treated in nitrogen. Defects configurations after testing are related to


DOI: 10.1021/acs.jpcc.7b06043
J. Phys. Chem. C 2017, 121, 17746−17755

samples oxidized with water, and the differences observed for the two materials suggest that water splitting proceeded through different pathways. We can put forward some hypotheses on the basis of recent theoretical and experimental studies regarding the stability and behavior of reduced $CeO_2(111)$ surface when interacting with water.[57] It is reported that large surface vacancy clusters are formed and stabilized via a "hydroxyl-vacancies model".[58] The coexistence of hydroxyl groups and vacancies at the subsurface of $CeO_{2-x}(111)$ favors the stabilization of vacancy dimers or trimers at the surface. Large clusters at the surface in turn favor the mobility of H in the bulk and a higher concentration of $Ce^{3+}$ at the surface.[59] The formation and presence of subsurface hydroxyl groups favor the H transfer between neighboring top-surface O and subsurface O rather than the direct surface diffusion of H among top-surface O, because of the lower energy barrier of the mechanism.[58] The high concentration of $Ce^{3+}$ at the surface, close to vacancy clusters, leads to a more significant charge modification of the neighboring surface O pushing more covalent electrons toward O. This would contribute to weaken the H−O bond and, consequently, benefit the process of H coupling, which requires O−H bond breaking, to form $H_2$.

The water splitting process involves surface reactions (i.e., adsorption/dissociation of water, ion/electron transfer on the surface, and association of H atoms and $H_2$ desorption) and incorporation of ions into the bulk. Recently, it has been demonstrated that in ceria−zirconia-based materials the surface oxygen-ions transfer, mediated by bulk oxygen vacancies, is fast and that the rate-determining step of reaction is related to the reduction of hydroxyl groups, and to the release of $H_2$, rather than due to the incorporation of ions into the bulk.[55,60]

Our results agree with the idea illustrated in Figure 6. The oxynitride phase contributes to create and stabilize large vacancy oxygen clusters[61] that at the first cycle can be easily hydroxilated (Figure 6A−C). The coexistence of these large clusters and hydroxyl groups helps in maintaining reduced the surface through a rapid replacement of vacancies from the bulk and an incorporation of hydroxyl groups into the subsurface

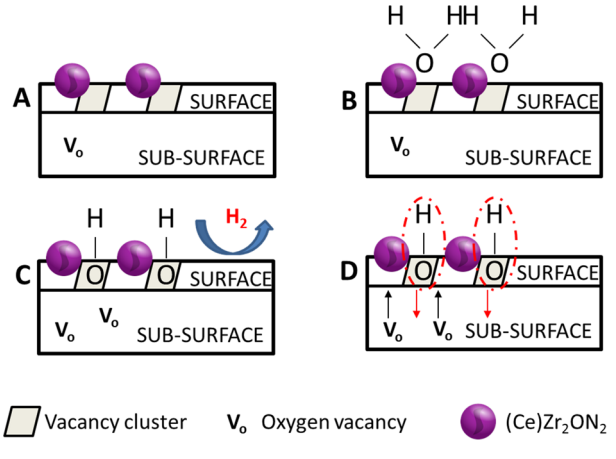


**Figure 6.** Surface activation mechanism of CZ80 doped with a zirconium oxynitride phase: (A) $(Ce)Zr_2ON_2$ contributes to form and stabilize large vacancy clusters (VC) on the surface; (B,C) water is adsorbed on VCs forming surface hydroxyl groups (OHs); and (D) hydroxylated clusters favor the incorporation of OHs into the subsurface layers and oxygen vacancies migration from the bulk; such configuration boosts the production of $H_2$ from the second redox cycle.

layers of the oxide (Figure 6D). This configuration contributes to boost the rate-determining step of water splitting to produce $H_2$, thus explaining the higher reactivity of the material treated in $N_2$ from the second cycle. In this view, the material treated under air lacks suitable centers to induce hydroxylation of subsurface, and the reaction will be limited at the surface with a less effective rearrangement of defects over cycles.

This study allows us also to clarify and explain the behavior of Zr-rich compositions such as $Ce_{0.15}Zr_{0.85}O_2$.[27] Despite that this latter composition is less thermally stable and shows a more significant surface segregation under nitrogen flow, the final composition at the outer part of the particles is similar to that observed for $Ce_{0.85}Zr_{0.15}O_2$. Figure 7 summarizes the main

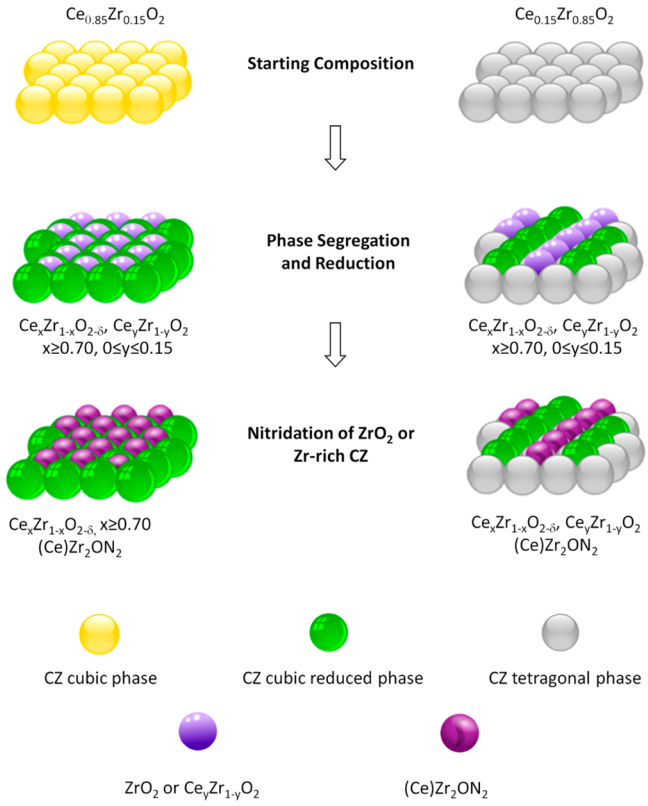


**Figure 7.** Schematic of segregation processes at 1300 °C in $N_2$ atmosphere of CZ85 and CZ15.

steps of the transformation for both the compositions trying to elucidate the reasons why ceria-rich and zirconia-rich materials show similar water splitting reactivity after thermal treatment in nitrogen and redox activation. It is worth noting that after thermal treatment, we end up with a surface phase arrangement that is characterized by the copresence of $Ce_xZr_{1-x}O_{2-\delta}$, $0.7 \leq x \leq 0.9$ and $Zr_2ON_2$, which is formed from the nitridation of segregated zirconia and is stable under redox cycles. The possibility that under our conditions the oxynitride phase might be doped with cerium cannot be excluded, and further investigations are requested to better address the nitridation mechanism and the stability of such phases.

## CONCLUSIONS

This study investigates the structural changes occurring on $Ce_{0.85}Zr_{0.15}O_2$ during thermochemical water splitting cycles. It is found that thermal aging in nitrogen atmosphere modifies the surface structure and composition of the materials by



DOI: 10.1021/acs.jpcc.7b06043
J. Phys. Chem. C 2017, 121, 17746−17755

promoting the segregation of a ceria−zirconia solid solution rich in ceria along with a zirconia−oxynitride phase, a fate that is similar to that found over zirconia-rich compositions. Positron annihilation lifetime spectroscopy measurements have shown that the oxynitride phase contributes to form large surface vacancy clusters with an appropriate defect configuration, which promotes charge transfer and H coupling, thus playing a pivotal role in boosting the production of $H_2$. Modification in the size distribution and number of structural defects can explain the different behavior when the material is treated under air atmosphere.

All of these findings suggest new approaches for the development and design of ceria-based materials for the two-step water splitting reaction and highlight the importance of engineering the surface defect structure/configuration of the material to obtain an efficient catalyst. In this regard, the role and the impact of nitridation process need to be further investigated.

## ■ ASSOCIATED CONTENT

### Supporting Information

The Supporting Information is available free of charge on the ACS Publications website at DOI: 10.1021/acs.jpcc.7b06043.

Reactivity tests, Raman spectra, XPS, HRTEM, and PALS spectra (PDF)

## ■ AUTHOR INFORMATION


### Corresponding Author

*Tel.: (+39)0432-558825. Fax: (+39)0432-558803. E-mail: marta.boaro@uniud.it.

### ORCID

Jordi Llorca: 0000-0002-7447-9582

Alessandro Trovarelli: 0000-0002-1396-4031

Marta Boaro: 0000-0002-6853-2965


### Notes

The authors declare no competing financial interest.

## ■ REFERENCES


(1) Miller, J. E.; McDaniel, A. H.; Allendorf, M. D. Considerations in the Design of Materials for Solar-Driven Fuel Production Using Metal-Oxide Thermochemical Cycles. *Adv. Energy Mater.* **2014**, *4*, 1−19.

(2) Agrafiotis, C.; Roeb, M.; Sattler, C. A Review on Solar Thermal Syngas Production via Redox Pair-Based Water/Carbon Dioxide Splitting Thermochemical Cycles. *Renewable Sustainable Energy Rev.* **2015**, *42*, 254−285.

(3) Scheffe, J. R.; Steinfeld, A. Oxygen Exchange Materials for Solar Thermochemical Splitting of $H_2O$ and $CO_2$: a Review. *Mater. Today* **2014**, *17*, 341−348.

(4) William, C. C.; Haile, M. S. Thermochemical Study of Ceria: Exploiting and Old Material for New Modes of Energy Conversion and $CO_2$ Mitigation. *Philos. Trans. R. Soc., A* **2010**, *368*, 3269−3294.

(5) Abanades, S.; Flamant, G. Thermochemical Hydrogen Production from a Two-Step Solar-Driven Water-Splitting Cycle Based on Cerium Oxides. *Sol. Energy* **2006**, *80*, 1611−1623.

(6) Chueh, W. C.; Falter, C.; Abbott, M.; Scipio, D.; Furler, P.; Haile, S. M.; Steinfeld, A. High-Flux Solar-Driven Thermochemical Dissociation of $CO_2$ and $H_2O$ Using non-Stoichiometric Ceria. *Science* **2010**, *330*, 1797−1801.

(7) Lapp, J.; Davidson, J. H.; Lipiński, W. Efficiency of two-step Solar Thermochemical Non-Stoichiometric Redox Cycles with Heat Recovery. *Energy* **2012**, *37*, 591−600.

(8) Siegel, N. P.; Miller, J. E.; Ermanoski, I.; Diver, R. B.; Stechel, E. B. Factors Affecting the Efficiency of Solar Driven Metal Oxide Thermochemical Cycles. *Ind. Eng. Chem. Res.* **2013**, *52*, 3276−3286.

(9) Bufin, B.; Call, F.; Lange, M.; Lübben, O.; Sattler, C.; Pitz-Paal, R.; Shvets, I. V. Thermodynamics of $CeO_2$ Thermochemical Fuel Production. *Energy Fuels* **2015**, *29*, 1001−1009.

(10) Scheffe, J. R.; Steinfeld, A. Thermodynamic Analysis of Cerium-Based Oxides for Solar Thermochemical Fuel Production. *Energy Fuels* **2012**, *26*, 1928−1936.

(11) Kim, T.; Vohs, J. M.; Gorte, R. J. Thermodynamic Investigation of the Redox Properties of Ceria-Zirconia Solid Solutions. *Ind. Eng. Chem. Res.* **2006**, *45*, 5561−5565.

(12) Hao, Y.; Yang, C.-K.; Haile, S. M. Ceria−Zirconia Solid Solutions ($Ce_{1-x}Zr_xO_{2-\delta}$, $x \leq 0.2$) for Solar Thermochemical Water Splitting: A Thermodynamic Study. *Chem. Mater.* **2014**, *26*, 6073−6082.

(13) Le Gal, A.; Abanades, S.; Bion, N.; Le Mercier, T.; Harlé, V. Reactivity of doped Ceria-Based Mixed Oxides for solar Thermochemical Hydrogen Generation via Two Step Water Splitting Cycles. *Energy Fuels* **2013**, *27*, 6068−6078.

(14) Le Gal, A.; Abanades, S. Dopants Incorporation in Ceria for Enhanced Water Splitting: Activity During Solar Thermochemical Hydrogen Generation. *J. Phys. Chem. C* **2012**, *116*, 13516−13523.

(15) Rudisill, S. G.; Venstrom, L. J.; Petkovich, N. D.; Quan, T.; Hein, N.; Boman, D. B.; Davidson, A.; Stein, J. H. Enhanced Oxidation Kinetics in Thermochemical Cycling of $CeO_2$ Through Template Porosity. *J. Phys. Chem. C* **2013**, *117*, 1692−1700.

(16) Lin, F. J.; Rothensteiner, M.; Alxneit, I.; van Bokhoven, J. A.; Wokaun, A. First Demonstration of Direct Hydrocarbon Fuel Production from Water and Carbon Dioxide by Solar-Driven Thermochemical Cycles Using Rhodium-Ceria. *Energy Environ. Sci.* **2016**, *9*, 2400−2409.

(17) Ruan, C.; Tan, Y.; Li, L.; Wang, J.; Liu, X.; Wang, X. A novel $CeO_{2-X}SnO_2/Ce_2Sn_2O_7$ Pyrochlore Cycles for Enhanced Solar Thermochemical Water Splitting. *AIChE J.* **2017**, *63*, 3450−3463.

(18) Kaneko, H.; Taku, S.; Tamaura, T. Reduction Reactivity of $CeO_2$−$ZrO_2$ Oxide Under High $O_2$ Partial Pressure in Two-Step Water Splitting Process. *Sol. Energy* **2011**, *85*, 2321−2330.

(19) Le Gal, A.; Abanades, S.; Flamant, G. $CO_2$ and $H_2O$ Splitting for Thermochemical Production of Solar Fuels using Non-Stoichiometric Ceria and Ceria/Zirconia Solid Solutions. *Energy Fuels* **2011**, *25*, 4836−4845.

(20) Le Gal, A.; Abanades, S. Catalytic Investigation of Ceria-Zirconia Solid Solutions for Solar Hydrogen Production. *Int. J. Hydrogen Energy* **2011**, *36*, 4739−4748.

(21) Bulfin, B.; Lange, M.; de Oliveira, L.; Roeb, M.; Sattler, C. Solar Thermochemical Hydrogen Production Using Ceria Zirconia Solid Solutions: Efficiency Analysis. *Int. J. Hydrogen Energy* **2016**, *41*, 19320−19328.

(22) Dasari, H. P.; Ahn, K.; Park, S.-Y.; Ji, H.-I.; Yoon, K. J.; Kim, B.-K.; Je, H.-J.; Lee, H.-W.; Lee, J.-H. Hydrogen Production from Water-Splitting Reaction Based on RE-Doped Ceria-Zirconia Solid-Solutions. *Int. J. Hydrogen Energy* **2011**, *38*, 6097−6103.

(23) Petkovich, N. D.; Rudisill, S. G.; Venstrom, L. J.; Boman, D. B.; Davidson, J. H.; Stein, A. Control of Heterogeneity in Nanostructured $Ce_{1-x}Zr_xO_2$ Binary Oxides for Enhanced Thermal Stability and Water Splitting Activity. *J. Phys. Chem. C* **2011**, *115*, 21022−21033.

(24) Wu, K.; Sun, L.-D.; Yan, C. H. Recent Progress in Well-Controlled Synthesis of Ceria-Based Nanocatalysts towards Enhanced Catalytic Performance. *Adv. Energy Mater.* **2016**, *6*, 1−46.

(25) Pappacena, A.; Boaro, M.; Šolcová, O.; Trovarelli, A. Ceria Based Materials with Enhanced OSC Properties for $H_2$ Production by Water Splitting Reaction Advances in Science and Technology. *Adv. Sci. Technol.* **2014**, *93*, 76−81.

(26) Boaro, M.; Desinan, S.; Abate, C.; Ferluga, M.; de Leitenburg, C.; Trovarelli, A. Study on Redox, Structural and Electrical Properties of $Ce_xZr_{1-x}O_2$ for Applications in SOFC Anodes. *J. Electrochem. Soc.* **2011**, *158*, P22−29.

(27) Pappacena, A.; Boaro, M.; Armelao, L.; Llorca, J.; Trovarelli, A. Water Splitting Reaction on $Ce_{0.15}Zr_{0.85}O_2$ Driven by Surface Heterogeneity. *Catal. Sci. Technol.* **2016**, *6*, 399−403.




DOI: 10.1021/acs.jpcc.7b06043
J. Phys. Chem. C 2017, 121, 17746−17755

(28) Pappacena, A.; Schermanz, K.; Sagar, A.; Aneggi, E.; Trovarelli, A. Development of a Modified Co-Precipitation Route for Thermally Resistant, High Surface Area Ceria-Zirconia Based Solid Solutions. *Stud. Surf. Sci. Catal.* **2010**, *175*, 835−838.
(29) Warren, B. E. *X-ray Diffraction*; Dover Publications Inc.: New York, 1990.
(30) Toby, B. H. J. EXPGUI, A Graphical User Interface for. *J. Appl. Crystallogr.* **2001**, *34*, 210−213.
(31) Larson, A. C.; Dreele, R. B. V. *General Structure Analysis System GSAS*; Los Alamos National Laboratory: Los Alamos, NM, 2000.
(32) Lowell, S.; Shields, J. E.; Thomas, M. A.; Thommes, M. *Characterization of Porous Solids and Powders: Surface Area, Pore Size and Density*; Kluwer Academic Publisher, Springer: Dordrecht, 2006.
(33) Briggs, D.; Seah, M. *Practical Surface Analysis*; Wiley: Chichester, 1990.
(34) Shirley, D. A. High-Resolution X-Ray Photoemission Spectrum of the Valence Bands of Gold. *Phys. Rev. B: Condens. Matter.* **1972**, *5*, 4709−4714.
(35) Moulder, J. F.; Stickle, W. F.; Sobol, P. E.; Bomben, K. D. In *Handbook of X-ray Photoelectron Spectroscopy, Physical Electronics*; Chastain, J., Ed.; Eden Prairie, MN, 1992.
(36) Hong, S. J.; Virkar, A. V. Lattice Parameters and Densities of Rare-Earth Oxide Doped Ceria Electrolytes. *J. Am. Ceram. Soc.* **1995**, *78*, 433−439.
(37) Zhang, F.; Chen, C.-H.; Hanson, J. C.; Robinson, R. D.; Herman, I. P.; Chan, S.-W. Phases in Ceria-Zirconia Binary Oxide (1-x)$CeO_2$-x$ZrO_2$ Nanoparticles: the Effect of Particle Size. *J. Am. Ceram. Soc.* **2006**, *89*, 1028−1036.
(38) Prustya, D.; Pathaka, A.; Mukherjeeb, M.; Mukherjeec, B.; Chowdhurya, A. TEM and XPS Studies on the Faceted Nanocrystals of $Ce_{0.8}Zr_{0.2}O_2$. *Mater. Charact.* **2015**, *100*, 31−35.
(39) Kaspar, J.; Fornasiero, P.; Balducci, G.; Di Monte, R.; Hickey, N.; Sergo, V. Effect of $ZrO_2$ Content on Textural and Structural Properties of $CeO_2$/$ZrO_2$ Solid Solutions Made by Citrate Complexation Route. *Inorg. Chim. Acta* **2003**, *349*, 217−226.
(40) Fornasiero, P.; Speghini, A.; Di Monte, R.; Bettinelli, M.; Kašpar, J.; Bigotto, A.; Sergo, V.; Graziani, M. Laser-Excited Luminescence of Trivalent Lanthanide Impurities and Local Structure in $CeO_2$-$ZrO_2$ Mixed Oxides. M. *Chem. Mater.* **2004**, *16*, 1938−1944.
(41) Sullivan, J. A.; Dulgheru, P.; Atribak, I.; Bueno-López, A.; García-García, A. Attempts at an in Situ Raman Study of Ceria/Zirconia Catalysts in PM Combustion. *Appl. Catal., B* **2011**, *108*−*109*, 134−139.
(42) Nolas, S.; Tsoukala, V. G.; Gayen, S. K. Electronic-Raman-Scattering Study of the Low-Lying Energy Levels of Trivalent Cerium-Doped Yttria. *Phys. Rev. B: Condens. Matter Mater. Phys.* **1994**, *50*, 150−158.
(43) Füglein, E.; Hock, R.; Lerch, M. Crystal Structure and High Temperature Behavior of $Zr_2ON_2$. *Z. Anorg. Allg. Chem.* **1997**, *623*, 304.
(44) Yang, M.; Rodgers, J. A.; Middler, L. C.; Oró-Solé, J.; Jorge, A. B.; Fuertes, A.; Attfield, J. P. Direct Solid-State Synthesis at High Pressures of New Mixed-Metal Oxynitrides: R$ZrO_2$N (R = Pr, Nd, and Sm). *Inorg. Chem.* **2009**, *48*, 11498−11500.
(45) Nelson, A. E.; Schulz, K. H. Surface Chemistry and Microstructural Analysis of $Ce_xZr_{1-x}O_{2-y}$ Model Catalyst Surfaces. *Appl. Surf. Sci.* **2003**, *210*, 206−221.
(46) Signore, M. A.; Rizzo, A.; Mirenghi, L.; Tangliente, M. A.; Cappello, A. Characterization of Zirconium Oxynitride Films Obtained by Radio Frequency Magnetron Reactive Sputtering. *Thin Solid Films* **2007**, *515*, 6798−6804.
(47) Roman, D.; Bernardi, J.; de Amorim, C.; de Souza, F.; Spinelli, A.; Giacomelli, C.; Figuero, C.; Baumvol, I.; Basso, R. Effect of Deposition Temperature on Microstructure and Corrosion Resistance of ZrN Thin Films Deposited by DC Reactive Magnetron Sputtering. *Mater. Chem. Phys.* **2011**, *130*, 147−153.
(48) Qiu, L.; Liu, F.; Zhao, L.; Ma, Y.; Yao, J. Comparative XPS Study of Surface Reduction for Nanocrystalline and Microcrystalline Ceria Powder. *Appl. Surf. Sci.* **2006**, *252*, 4931−4935.
(49) Chakraverty, S.; Mitra, S.; Mandal, K.; Nambissan, P. M. G.; Chattopadhyay, S. Positron Annihilation Studies of some Anomalous Features of $NiFe_2O_4$ Nanocrystals Grown in $SiO_2$. *Phys. Rev. B: Condens. Matter Mater. Phys.* **2005**, *71*, 024115.
(50) Dutta, S.; Chattopadhyay, S.; Jana, D.; Banerjee, A.; Manik, S.; Pradhan, S. K.; Sutradhar, M.; Sarkar, A. Annealing Effect on Nano-ZnO Powder Studied from Positron Lifetime and Optical Absorption Spectroscopy. *J. Appl. Phys.* **2006**, *100*, 114328.
(51) Sanyal, D.; Banerjee, D.; De, U. $(Bi_{0.92}Pb_{0.17})_2Sr_{1.91}Ca_{2.03}Cu_{3.06}O_{10+\delta}$ Superconductors from 30 to 300 K by Positron-Lifetime Measurements. *Phys. Rev. B: Condens. Matter Mater. Phys.* **1998**, *58*, 15226.
(52) Liu, X.; Zhou, K.; Wang, L.; Wang, B.; Li, Y. Oxygen Vacancy Clusters Promoting Reducibility and Activity of Ceria Nanorods. *J. Am. Chem. Soc.* **2009**, *131*, 3140−3141.
(53) Prochazka, I.; Cizek, J.; Melikhova, O.; Konstantinova, E. T.; Danilenko, I. A.; Yashehisyn, I. A. Positron Annihilation Study of Zirconia Nanopowders and Nanoceramics Stabilized by Magnesia and Ceria. *J. Am. Ceram. Soc.* **2014**, *97*, 982−989.
(54) Kong, M.; Li, Y.; Chen, X.; Tian, T.; Fang, P.; Zheng, F.; Zhao, X. Tuning the Relative Concentration Ratio of Bulk Defects to Surface Defects in $TiO_2$ Nanocrystals Leads to High Photocatalytic Efficiency. *J. Am. Chem. Soc.* **2011**, *133*, 16414−16417.
(55) Zhao, Z.; Uddi, M.; Tsvetkov, N.; Yildiz, B.; Ghoniem, A. F. Redox Kinetics Study of Fuel Reduced Ceria for Chemical-Looping Water Splitting. *J. Phys. Chem. C* **2016**, *120*, 16271−16269.
(56) Lerch, M. Nitridation of Zirconia. *J. Am. Ceram. Soc.* **1996**, *79*, 2641−2644.
(57) Chen, B.; Ma, Y.; Ding, L.; Xu, L.; Wu, Z.; Yuan, Q.; Huang, W. Reactivity of Hydroxyls and Water on a $CeO_2$(111) Thin Film Surface: The Role of Oxygen Vacancy. *J. Phys. Chem. C* **2013**, *117*, 5800−5810.
(58) Wu, X. P.; Gong, X.-Q. Clustering of Oxygen Vacancies at $CeO_2$(111): Critical Role of Hydroxyls. *Phys. Rev. Lett.* **2016**, *116*, 086102, 1−6.
(59) Wu, X. P.; Gong, X.-Q.; Lu, G. Role of Oxygen Vacancies in the Surface Evolution of $H_2$ at $CeO_2$(111): a Charge Modification Effect. *Phys. Chem. Chem. Phys.* **2015**, *17*, 3544−3549.
(60) Feng, A.; Galaby, F. E.; Ye, X.; Shen, Z.-X.; Chueh, W. C. Fast Vacancy-Mediated Oxygen Ion Incorporation Across the Ceria-Gas Electrochemical Interface. *Nat. Commun.* **2014**, *5*, 1−8.
(61) Attfield, J. P. Principles and Applications of Anion Order in Solid Oxynitrides. *Cryst. Growth Des.* **2013**, *13*, 4623−4629.


DOI: 10.1021/acs.jpcc.7b06043
*J. Phys. Chem. C* 2017, 121, 17746−17755